Journal of Colloid and Interface Science 725 (2027) 141519

Contents lists available at ScienceDirect

Journal of Colloid And Interface Science

journal homepage: www.elsevier.com/locate/jcis

Electronic regulation of electrochemical reconstruction via a Ce^{3+}/Ce^{4+} electron buffer for efficient alkaline water splitting

Haoran Yin [a], Linyu Chen [a], Linlin Huang [a], Tayirjan Taylor Isimjan [c,*], Dandan Cai [b,*], Xiulin Yang [a,*]

[a] Guangxi Key Laboratory of Low Carbon Energy Materials, School of Chemistry and Pharmaceutical Sciences, Guangxi Normal University, Guilin 541004, Guangxi, China
[b] National Engineering Research Center for Carbohydrate Synthesis, Key Laboratory of Fluorine and Silicon for Energy Materials and Chemistry of Ministry of Education, School of Chemical Engineering, Jiangxi Normal University, Nanchang 330022, China
[c] Saudi Arabia Basic Industries Corporation (SABIC) at King Abdullah University of Science and Technology (KAUST), Thuwal 23955-6900, Saudi Arabia

HIGHLIGHTS

- Ce^{3+}/Ce^{4+} redox drives stable β-NiOOH formation in NiCe NDC.
- Ce 4f reservoirs tune Ni d-band center, lowering OER barrier.
- NiCe NDC/CP exhibits good OER activity and long-term stability.
- 20 MW electrolyzer assessment predicts H_2 cost ~USD 5.40 kg^{-1}.

GRAPHICAL ABSTRACT

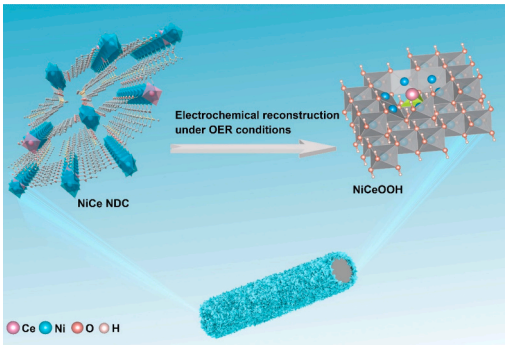

ARTICLE INFO

Keywords:
Metal organic framework
Rare earth metals doping
Synergistic effect
Self-reconstruction
Water splitting

ABSTRACT

The rational regulation of electrochemical reconstruction is a promising route to high-performance oxygen evolution reaction (OER) electrocatalysts, yet the underlying electronic mechanisms and their technological relevance remain elusive. Herein, a Ce-doped Ni-based metal organic framework (NiCe NDC) precatalyst is fabricated via a facile one-step solvothermal method. The reversible Ce^{3+}/Ce^{4+} redox pair acts as a dynamic electron-buffering center, and the strong Ni 3d–O 2p–Ce 4f orbital coupling induces controllable reconstruction into stable β-NiOOH, while inhibiting the over-oxidation and structural deterioration of active phases. In situ Raman spectroscopy and X-ray photoelectron spectroscopy verify the optimized reconstruction kinetics and reversible Ce valence evolution, while density functional theory (DFT) calculations confirm that near-Fermi-level Ce 4f states serve as electron reservoirs to modulate the Ni d-band center, enrich electronic density at the Fermi level, and reduce the free-energy barrier of the rate-determining *O to *OOH step. Optimized NiCe NDC delivers superior alkaline OER performance with a low overpotential of 194 mV at 10 mA cm^{-2}, a small Tafel slope of 61.8 mV dec^{-1}, and long-term stability over 100 h at 100 mA cm^{-2}. Coupled with a Pt/C cathode, the assembled overall water-splitting electrolyzer achieves current densities of 10–1000 mA cm^{-1} under low cell voltages of

* Corresponding authors
E-mail addresses: isimjant@sabic.com (T.T. Isimjan), caidandan86@163.com (D. Cai), xlyang@gxnu.edu.cn (X. Yang).

https://doi.org/10.1016/j.jcis.2026.141519
Received 6 August 2026; Received in revised form 31 August 2026; Accepted 2 September 2026
Available online 5 September 2026

1.42–1.90 V. A techno-economic assessment (TEA) of a 20 MW alkaline electrolyzer estimates a levelized cost of hydrogen (LCOH) of ~USD 5.40 $kg^{-1}H_2$. This work reveals the electronic mechanism of rare-earth-regulated reconstruction and provides a feasible strategy for designing advanced OER catalysts toward industrial green hydrogen production.

1. Introduction

Hydrogen produced by water electrolysis is widely recognized as one of the most promising clean energy carriers for achieving carbon neutrality and enabling the large-scale integration of renewable electricity into future energy systems [1–3]. Among the half-reactions involved in water electrolysis, the oxygen evolution reaction (OER) remains the principal kinetic bottleneck because of its complex four-electron transfer pathway and the unfavorable adsorption energies of oxygen-containing intermediates [4–7]. For this reason, designing electrocatalysts combining high OER activity and long operational stability is critical to boost energy utilization efficiency and advance practical commercial implementation of electrolytic hydrogen production.

To date, noble-metal oxides, particularly IrO_2 and RuO_2, have remained the benchmark OER catalysts because of their outstanding intrinsic activity and stability under alkaline conditions [8,9]. However, their scarcity, high cost, and supply-chain limitations significantly impede the widespread deployment of large-scale water electrolyzers [10–12]. Nevertheless, the low terrestrial abundance, prohibitive price and vulnerable supply of these precious metals constitute major obstacles to their industrial-scale implementation in water-electrolysis systems. Consequently, enormous research attention has been directed toward non-precious transition-metal alternatives that can match noble-metal performance while relying on geologically abundant elements. Within this category, nickel-based compounds stand out as particularly compelling candidates. Their appeal stems from a combination of encouraging OER reactivity in alkaline media, rich natural reserves, economic affordability and readily tunable electronic configurations. Accumulating experimental evidence and theoretical analyses have converged on the conclusion that nickel oxyhydroxide (NiOOH), formed via in-situ electrochemical reconstruction, constitutes the genuine catalytically active phase under alkaline OER conditions, wherein surface-exposed Ni centers directly mediate the adsorption and subsequent conversion of oxygenated reaction intermediates [13].

Depending on the crystal structure and interlayer composition, NiOOH generally exists in three polymorphs: α-, β-, and γ-NiOOH [14,15]. Each phase exhibits distinct advantages and limitations. α-NiOOH possesses a relatively large interlayer spacing and abundant surface hydroxyl groups, resulting in high intrinsic catalytic activity, but it readily undergoes irreversible phase transformation during prolonged anodic polarization. β-NiOOH exhibits a well-ordered crystal structure and superior structural stability; however, its relatively low active-site density and moderate electronic conductivity limit its intrinsic activity, particularly at high current densities. γ-NiOOH combines high nickel valence states with abundant structural defects and therefore demonstrates excellent catalytic activity, but it often suffers from severe amorphization and structural degradation during long-term operation [16,17]. Consequently, simultaneously achieving high activity and long-term structural stability remains one of the central challenges in designing Ni-based OER catalysts.

Directly synthesized NiOOH frequently suffers from particle agglomeration, limited active-site exposure, and poor control over phase composition, making it difficult to optimize both activity and durability [18]. Recently, nickel-based metal organic frameworks (Ni MOFs) have emerged as highly attractive pre-catalysts because they undergo controlled electrochemical reconstruction into catalytically active NiOOH during OER. Compared with conventional synthesis routes, MOF precursors possess highly ordered porous architectures, tunable coordination environments, and uniform metal distributions, enabling precise regulation of the reconstruction process [19–21]. Furthermore, rational engineering of precursor composition through heteroatom doping provides an effective strategy for controlling reconstruction kinetics, phase evolution, defect generation, and active-site formation, thereby significantly improving catalytic performance.

Among the various modification strategies, metal doping has proven particularly effective for regulating the reconstruction behavior of MOF-derived electrocatalysts [22–26]. Depending on their catalytic roles, dopants generally function through two distinct mechanisms. The first involves direct participation in the OER process by forming bimetallic active centers that optimize the adsorption energies of reaction intermediates and lower the energy barrier of the rate-determining step. Typical examples include Fe and Co dopants, which generate synergistic catalytic sites with Ni. The second mechanism involves dopants acting primarily as electronic or structural promoters rather than direct catalytic centers. These promoter elements regulate the electronic structure, lattice distortion, defect concentration, and reconstruction pathway of the host catalyst, thereby facilitating the formation of highly active and structurally stable NiOOH phases [27,28].

Rare-earth species hold great promise as doping promoters, which is rooted in their distinctive 4*f* orbital features and reversible multivalence. Their variable oxidation states enable dynamic electron buffering that continuously regulates the electron density and valence evolution of neighboring transition-metal centers during electrocatalysis [29,30]. In addition, their relatively large ionic radio induces lattice distortion and defect formation, providing additional opportunities for electronic modulation and active-site optimization. Among them, cerium has attracted considerable interest because the reversible Ce^{3+}/Ce^{4+} redox couple behaves as a dynamic electron reservoir-or "electron pump"-capable of continuously accepting and donating electrons during electrochemical operation [31–33]. Previous studies have demonstrated that Ce incorporation can effectively regulate the electronic structure of nickel-based catalysts and promote the formation of active NiOOH species [25]. Nevertheless, despite these advances, the fundamental mechanism by which the Ce-mediated electron-pump effect governs the electrochemical reconstruction of Ni-MOF pre-catalysts remains poorly understood. In particular, the relationships among orbital coupling, microscopic energy-level alignment, reconstruction kinetics, active-phase evolution, and catalytic stability have yet to be systematically established.

Herein, we report a series of Ce-doped Ni NDC metal organic framework pre-catalysts synthesized through a one-pot solvothermal strategy, in which Ce ions are incorporated into the Ni NDC lattice to function as electron-pump dopants (NiCe NDC). Benefiting from strong orbital coupling among Ni 3*d*, O 2*p*, and Ce 4*f* orbitals, the reversible Ce^{3+}/Ce^{4+} redox couple dynamically regulates the electrochemical reconstruction process, promoting the directed formation of structurally stable β-NiOOH with abundant OER-active sites while suppressing excessive oxidation and structural degradation of Ni centers during anodic operation. In situ electrochemical Raman spectroscopy directly reveals the reconstruction kinetics and phase evolution, whereas density functional theory calculations demonstrate that the Ce 4*f* impurity states crossing the Fermi level serve as reversible electron reservoirs that modulate the electron density of Ni active sites and lower the free-energy barrier of the rate-determining *O to *OOH conversion step. Beyond elucidating the electronic origin of this Ce electron-pump effect, this work incorporates a preliminary techno-economic assessment to evaluate the catalyst's practical potential for industrial hydrogen

production. By coupling catalytic performance with electrolyzer energy consumption and hydrogen cost, the combined analyses establish an electronic-structure-guided strategy for high-performance Ni-based OER electrocatalysts and offer insights into economically viable green hydrogen production.

2. Experimental

2.1. Materials

All chemicals were employed as-received without extra purification. Naphthalene-2,6-dicarboxylic acid (H_2NDC, 98%), $NiCl_2 \cdot 6H_2O$ (98%), Ce $(Ac)_3 \cdot 4H_2O$ (99%) and KOH (95%) were supplied by Aladdin Chemical Reagent Co. Ltd. Absolute ethanol (99.7%), methanol (99.7%) and DMF (98%) were obtained from Xilong Chemical Reagent Co. Ltd. Toray Co. Ltd. provided carbon fiber paper (CP), which was cut into 2 cm × 1 cm pieces for electrochemical tests. Commercial 20 wt% Pt/C catalyst and 5 wt% Nafion solution were purchased from Alfa Aesar. The RuO_2 reference catalyst was synthesized via direct pyrolysis of $RuCl_3 \cdot 3H_2O$ (37%, Inno-chem) under air atmosphere at 400 °C.

2.2. Treatment of CP

Carbon fiber paper was pre-treated by hydrothermal oxidation using 68 wt% HNO_3 solution. The hydrothermal treatment was carried out at 120 °C over 180 min. Afterwards, the substrate was thoroughly rinsed sequentially using deionized water and absolute ethanol.

2.3. Synthesis of Ni NDC/CP, NiCe NDC/CP, RuO_2/CP and Pt/C/CP

$NiCl_2 \cdot 6H_2O$ (1 mmol) together with 0.75 mmol H_2NDC were dissolved in 15 mL mixed solvent with equal-volume DMF and MeOH. The homogeneous solution was transferred into a 25 mL Teflon-lined autoclave containing two pieces of pre-treated CP substrate. After sealing, solvothermal reaction proceeded at 120 °C for 9 h. Upon natural cooling to ambient temperature, the samples were rinsed three times using absolute ethanol and dried at 60 °C over 8 h.

NiCe NDC/CP was prepared under identical solvothermal conditions, where $Ce(Ac)_3 \cdot 4H_2O$ was incorporated while keeping total metal-salt loading fixed at 1 mmol. A series of doped catalysts with varied Ni/Ce stoichiometries were obtained, denoted as $Ni_{0.98}Ce_{0.02}$ NDC/CP, $Ni_{0.95}Ce_{0.05}$ NDC/CP, NiCe NDC/CP and $Ni_{0.91}Ce_{0.09}$ NDC/CP.

For reference electrodes, RuO_2 and Pt/C catalysts were deposited onto CP via drop-casting. 2 mg of catalyst powder was dispersed in 250 μL mixed solution (deionized water / isopropyl alcohol, 1:1), followed by adding 25 μL 5 wt% Nafion solution as binder. The well-mixed ink was cast onto CP substrates with dimensions of 1 cm × 0.5 cm.

2.4. Characterization

Powder X-ray diffraction (PXRD, Rigaku D/Max-3c, Cu-Kα, λ = 1.54056 Å) was applied to analyse crystal structures. Sample morphology and elemental distribution were characterized by scanning electron microscopy (SEM, Gemini Sigma 300) and transmission electron microscopy (TEM, Talos F200S, TFS, USA) equipped with EDS and SAED modules. Atomic-force microscopy (AFM, Dimension ICON, Bruker, USA) was used to determine the thickness of nanosheet-like samples. Surface elemental composition and valence states were probed by X-ray photoelectron spectroscopy (XPS, ESCA-LAB250, Al Kα source, 1486.6 eV). Bulk metal contents were quantified by ICP-MS (PerkinElmer, FLexar-NexION300X). Ex-situ Raman measurements were collected on Renishaw inVia instrument (514 nm laser). In-situ Raman tests were carried out on InVia Qontor spectrometer coupled with a Gaoss Union C031–1 electrochemical cell. Contact-angle measurements were performed using a dataphysics OCA 15EC tester to evaluate surface wettability.

2.5. Electrochemical measurements

Electrochemical measurements were conducted using the CHI760E electrochemical workstation (Chenhua Instrument, Shanghai, China) with a standard three-electrode system (The as-synthesized catalyst was acted as integrated working electrode, carbon rod and Hg/HgO were used as the counter electrode and the reference electrode, respectively) in 1.0 M KOH aqueous solution. All electrode potentials were converted to reversible hydrogen electrode (RHE) electrode potentials by the Nernst equation: $E_{vs.\ RHE} = E_{vs.Hg/HgO} + 0.059pH + 0.098$ V. The oxygen evolution overpotential (η) was calculated according to the following formula: $\eta\ (V) = E_{vs.\ RHE} - 1.23$ V. Linear sweep voltammetry (LSV) was performed at a scan rate of 1 mV s^{-1} from 1.2 V to 0.3 V. All LSV polarization curves were corrected using 95% *iR* compensation. The Tafel slope was plotted by converting the LSV curve according to the following formula: $\eta = a + b \log j$, where η was the overpotential (mV), j was the corresponding current density (mA cm^{-2}), b was the Tafel slope (mV dec^{-1}). Electrochemical ac impedance (EIS) was performed in the frequency range 10,000 Hz–0.01 kHz with an amplitude of 5 mV. A typical R(R-CPE) circuit was adopted to fit the impedance data, where R_s represents solution resistance, R_{ct} corresponds to charge-transfer resistance, and CPE is the constant-phase element accounting for surface inhomogeneity of electrocatalysts. Chronopotentiometry (CP, no *iR* compensation) to the stability of the active electrode.

The value of TOF is calculated according to the following formula:

$$TOF = \frac{jA}{4nF}$$

Here, A (cm^2) represents the geometric area of the CFP. The number 4 means the four electrons transfer in OER and F is equal to the constant of 96,485.3C mol^{-1}. n represents the number of mole metal ions in the samples.

The ECSA was assessed by C_{dl} and the corresponding curves of the catalysts were measured by cyclic voltammetry (CV) where no Faradaic process occurs (0.95–1.05 V *vs.* RHE) at varied scan rates of 10, 20, 30, 40 and 50 mV s^{-1}. The linear slope of the capacitive current versus scan rate was equivalent to double C_{dl}. The formula for calculating C_{dl} is: $C_{dl} = (j_a - j_c)/(2 \times \nu)$, where j_a and j_c correspond to the anodic and cathodic current density, respectively, and ν represents the scanning rate. The ECSA of catalyst was calculated using the expression: $A_{ECSA} = C_{dl}/C_s$, where the value of C_s is generally in the range of 20 to 60 μF cm^{-2}. An average value of C_s was 40 μF cm^{-2}.

For electrochemical in-situ Raman spectra measurements: The laser excitation wavelength used was 532 nm and the exposure time was set to 10 min for each spectrum. The as-prepared catalyst, carbon rod and Ag/AgCl electrode were served as the working electrode, counter electrode and reference electrode, respectively. The evolution of catalyst was monitored by gathering Raman spectra at constant potential ranging from 1.1 to 1.5 V (vs. RHE).

2.6. DFT calculation

Spin-polarized DFT simulations were implemented within Vienna ab-initio simulation package (VASP) [34,35]. Exchange-correlation functional GGA-PBE was chosen to describe electronic interactions [36]. Projector-augmented-wave (PAW) pseudopotentials were used for ion-electron treatment [37]. During geometry relaxation, atomic positions were optimized until Hellmann-Feynman forces on every atom dropped below 0.02 eV·$Å^{-1}$. Self-consistent Kohn-Sham iterations converged at an energy threshold of 10^{-6} eV.

2.7. Techno-economic analysis

A preliminary techno-economic assessment (TEA) was conducted to estimate the levelized cost of hydrogen (LCOH) produced in a medium-

scale alkaline water-electrolysis plant incorporating the developed noble-metal-free NiCe NDC catalyst. And the detailed can be seen in the supporting information.

3. Results and discussion

3.1. Structural and morphological characterizations

The synthesis procedure of NiCe NDC/CP is illustrated in Fig. 1a. NiCe NDC nanosheets were directly grown on carbon paper (CP) through a facile one-step solvothermal method using $NiCl_2{\cdot}6H_2O$, $Ce(Ac)_3{\cdot}4H_2O$, and H_2NDC as the metal precursors and organic ligand, respectively. Because Ce possesses a lower electronegativity and a larger ionic radius than Ni, introducing Ce into the Ni NDC is expected to modify the local electronic environment and induce slight lattice distortion while preserving the overall coordination structure at low doping concentrations. The crystal structures of the synthesized samples were first examined by X-ray diffraction (XRD). As shown in Fig. 1b, all samples exhibit two intense diffraction peaks at approximately 26.6° and 54.8°, corresponding to the carbon paper substrate (PDF# 26-1077). The diffraction pattern of pristine Ni NDC/CP agrees well with the simulated Ni-MOF structure, and no additional crystalline impurity phases are observed after Ce incorporation, indicating that low-level Ce doping does not alter the crystal framework of Ni NDC [38]. Notably, the characteristic diffraction peak near 7.5° shifts slightly toward lower diffraction angles after Ce incorporation. This shift is reasonably attributed to lattice expansion arising from the substitution of Ni^{2+} (0.072 nm) by the relatively larger Ce^{3+} (0.103 nm) and Ce^{4+} (0.092 nm) ions, suggesting successful incorporation of Ce into the Ni NDC lattice rather than the formation of separate Ce-containing crystalline phases [39]. Raman spectroscopy was also used to examine the framework coordination environment (Fig. 1c). Ni NDC/CP and NiCe NDC/CP exhibit ligand-related vibrational features spanning 1200–1800 cm^{-1}. The 1608 and 1420 cm^{-1} peaks arise from asymmetric and symmetric stretching of coordinated carboxylate moieties, validating metal-linker coordination. Minimal spectral variation after Ce incorporation demonstrates the retention of the original MOF backbone.

The morphology and microstructure of the catalysts were characterized using scanning electron microscopy (SEM), atomic force microscopy (AFM), and high-resolution transmission electron microscopy (HR-TEM). As shown in Fig. 1d, the optimized NiCe NDC/CP consists of interconnected ultrathin nanosheets uniformly covering the carbon paper substrate. Compared with pristine Ni NDC/CP (**Fig. S1**), Ce incorporation does not noticeably alter the overall nanosheet morphology, indicating that the solvothermal growth process remains largely unaffected by low-level Ce doping. AFM measurements reveal an average nanosheet thickness of approximately 4.3 nm (Fig. 1e). Such ultrathin two-dimensional architectures are advantageous for electrocatalysis because they expose abundant active sites, shorten ion-transport pathways, and facilitate interfacial charge transfer during

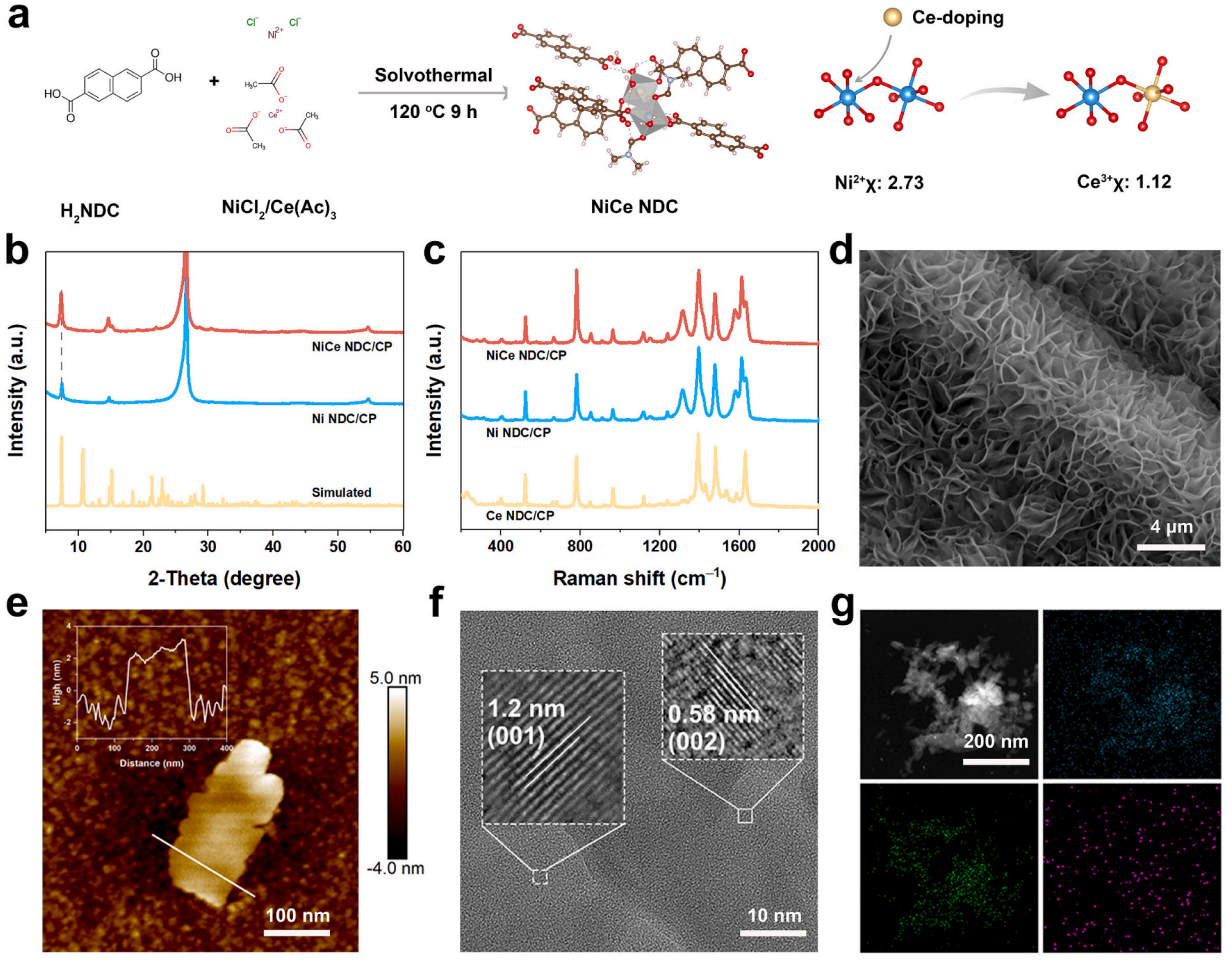

Fig. 1. (a) Synthetic route toward NiCe NDC. (b) Powder X-ray diffraction (XRD) patterns of the simulated Ni metal organic framework (Ni MOF), together with NiCe NDC/CP, Ni NDC/CP and Ce NDC/CP. (c–f) Morphological and structural characterizations of NiCe-NDC/CP: (c) scanning electron microscopy (SEM), (d) atomic force microscopy (AFM), (e) transmission electron microscopy (TEM) and (f) high-resolution transmission electron microscopy (HR-TEM) images. (g) Energy-dispersive X-ray spectroscopy (EDS) elemental mapping of NiCe NDC/CP, with O, Ni and Ce displayed in cyan, green and magenta, respectively. (For interpretation of the references to colour in this figure legend, the reader is referred to the web version of this article.)

the OER process. For comparison, Ce NDC/CP was also synthesized. Its XRD and Raman spectra agree well with those of previously reported Ce MOF materials, while SEM images reveal a distinct flower-like morphology assembled from nanosheets (**Figs. S2 and S3**), highlighting the structural differences between the Ce-MOF and NiCe NDC systems. HR-TEM analysis of NiCe NDC/CP (Fig. 1f) reveals lattice spacings of approximately 1.20 and 0.58 nm, corresponding to the (001) and (002) planes of the Ni-MOF, respectively. Elemental mapping by energy-dispersive X-ray spectroscopy (EDS) demonstrates the homogeneous distribution of Ni, Ce, and O throughout the nanosheets (Fig. 1g), indicating successful incorporation of Ce into the catalyst. Furthermore, inductively coupled plasma mass spectrometry (ICP-MS) confirms that the measured Ni/Ce atomic ratios closely agree with the designed precursor compositions (**Table S1**), providing quantitative verification of the catalyst composition.

The chemical states and electronic interactions of the catalysts were investigated by X-ray photoelectron spectroscopy (XPS). As shown in Fig. 2a, the survey spectrum of NiCe NDC/CP displays characteristic signals corresponding to C, O, Ni, and Ce, confirming the successful incorporation of Ce into the Ni NDC. The high-resolution Ni 2*p* spectrum (Fig. 2b) exhibits two dominant peaks located at 856.26 and 873.90 eV, which are assigned to the Ni $2p_{3/2}$ and Ni $2p_{1/2}$ levels of Ni^{2+}, respectively [26,40]. Compared with pristine Ni NDC/CP, the Ni $2p_{3/2}$ peak of NiCe NDC/CP shifts by approximately 0.12 eV toward lower binding energy, indicating an increase in the electron density around the Ni centers after Ce incorporation [41,42]. This observation suggests the existence of strong electronic interactions between Ce and neighboring Ni sites, implying that Ce doping effectively modulates the local electronic structure of the active centers. The Ce 3*d* spectrum (Fig. 2c) confirms the coexistence of Ce^{3+} and Ce^{4+} species, consistent with previous reports [43,44]. The mixed-valence Ce^{3+}/Ce^{4+} redox couple provides the electronic basis for a dynamic electron-buffering mechanism during electrochemical reconstruction and OER operation. Unlike conventional transition-metal dopants that primarily act as additional catalytic sites, Ce functions as an electronic promoter capable of reversibly accepting and donating electrons according to the local electrochemical environment. This electronic regulation can be rationalized from the perspective of orbital interactions. In pristine Ni NDC, Ni^{2+} possesses a $3d^8$ electronic configuration. Under an octahedral crystal field, the occupied Ni e_g orbitals strongly interact with the bridging O 2*p* orbitals, resulting in relatively localized electronic states around the Ni centers. After Ce incorporation, the formation of Ni-O-Ce bridges introduces low-lying Ce 4*f* states that electronically couple with the O 2*p* orbitals [45]. This orbital coupling facilitates charge delocalization across the Ni-O-Ce network and reduces electron localization at Ni sites, thereby modulating the local electronic structure of Ni and accounting for the experimentally observed decrease in Ni binding energy (Fig. 2d). As discussed later by density functional theory calculations, the Ce 4*f* states located near the Fermi level function as reversible electron reservoirs that dynamically regulate the electron density of the Ni active centers during electrochemical operation [46,47]. The interfacial wettability of the electrodes was further evaluated by static water contact-angle measurements (Fig. 2e). NiCe NDC/CP and Ni NDC/CP exhibit contact angles of 13.54° and 33.78°, respectively. The introduction of Ce reduces the contact angle, further improving surface hydrophilicity. Both electrodes remain highly hydrophilic, guaranteeing efficient electrolyte penetration and sufficient accessibility of active sites during OER.

3.2. *Electrocatalytic OER performance*

The oxygen evolution reaction (OER) activities of the as-prepared catalysts supported on carbon paper were systematically evaluated in 1.0 M KOH using a standard three-electrode configuration, with commercial RuO_2/CP serving as the benchmark catalyst. The optimized NiCe NDC/CP exhibits the highest catalytic activity among all samples, requiring an overpotential of only 194 mV to achieve a current density of 10 mA cm^{-2} (Fig. 3a **and Figs. S4 and S5**). This value is substantially lower than those of pristine Ni NDC/CP (277 mV) and commercial RuO_2/CP, demonstrating the remarkable promotional effect of Ce

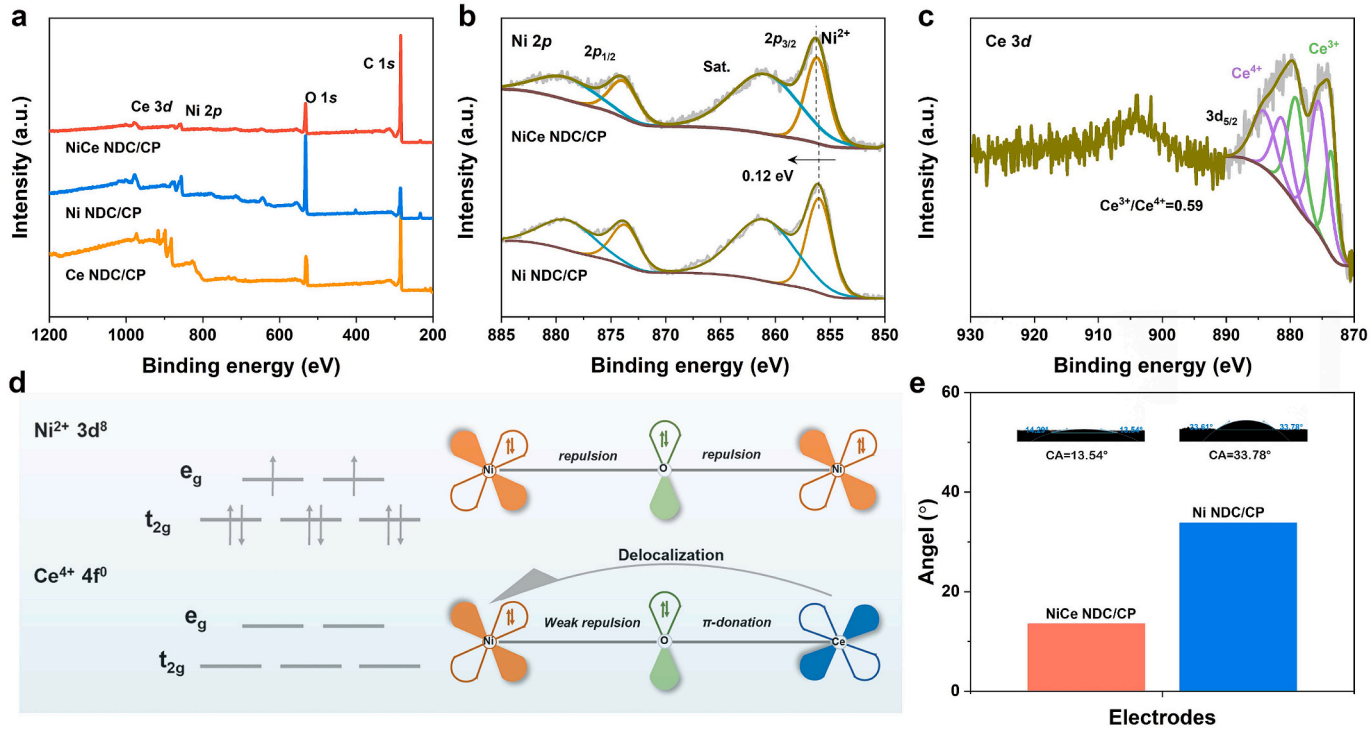

Fig. 2. (a) X-ray photoelectron spectroscopy (XPS) full-range survey profiles for NiCe NDC/CP, Ni NDC/CP and Ce NDC/CP. High-resolution XPS signals of (b) Ni 2*p* and (c) Ce 3*d* are compared between NiCe NDC/CP and Ni NDC/CP. (d) Schematic illustration depicting the electronic coupling among Ni, Ce and O within NiCe NDC/CP. (e) Water contact-angle measurements acquired for Ni NDC/CP and NiCe NDC/CP.

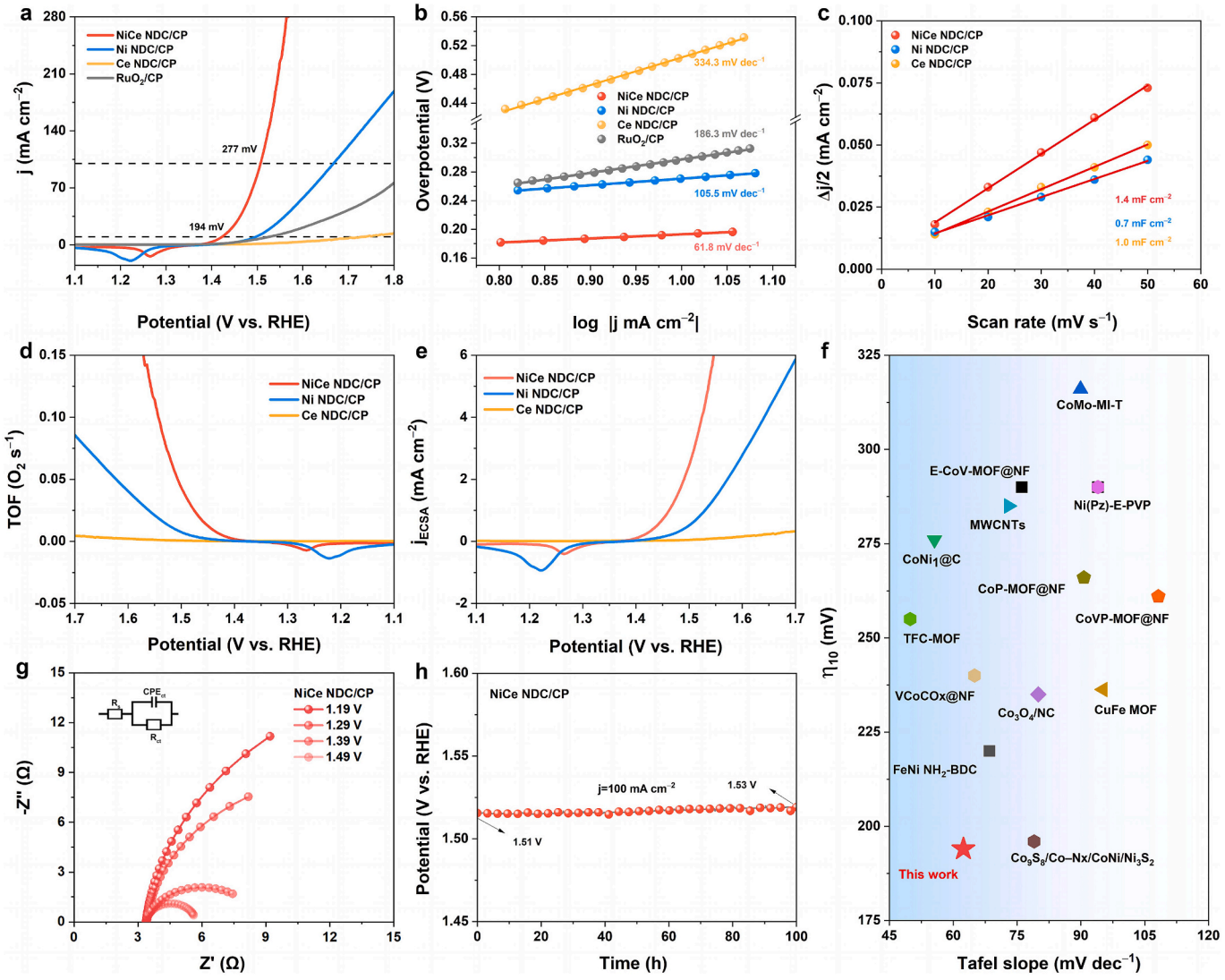

Fig. 3. (a) Linear sweep voltammetry (LSV) profiles for RuO_2/CP, NiCe NDC/CP, Ni NDC/CP and Ce NDC/CP measured in 1.0 M KOH. (b) Corresponding Tafel slopes extracted from the above LSV datasets. (c) Calculated double-layer capacitance (C_{dl}) values, (d) turnover frequency (TOF) parameters, and (e) electrochemical active surface area (ECSA)-normalized LSV curves. (f) Comparison of the overpotential at 10 mA cm^{-2} and Tafel slopes with previously reported metal organic framework-based catalysts. (g) Nyquist plots of NiCe NDC/CP at different applied potentials (vs. reversible hydrogen electrode (RHE)) in 1.0 M KOH. (h) Chronopotentiometry response acquired for NiCe NDC/CP.

incorporation on the OER performance. In contrast, Ce-NDC/CP displays negligible catalytic activity, as evidenced by its substantially delayed onset potential and slow increase in current density with increasing applied potential. Combined with the SEM observations, which reveal severe particle aggregation and poor in situ growth on the carbon paper substrate, these results indicate that Ce-based species are not intrinsically active OER catalysts. Instead, Ce primarily functions as an electronic and structural promoter within the NiCe NDC framework, where it modifies the local electronic environment and regulates the evolution of the active phase rather than directly serving as the catalytic center.

To further elucidate the origin of the enhanced activity, the reaction kinetics were investigated using Tafel analysis and electrochemical impedance spectroscopy (EIS). NiCe NDC/CP exhibits the smallest Tafel slope of 61.8 mV dec^{-1} together with the lowest charge-transfer resistance among all catalysts, indicating substantially accelerated interfacial electron-transfer kinetics and more favorable OER reaction pathways (Fig. 3b **and Fig. S6**). These results demonstrate that incorporating Ce not only enhances the intrinsic activity of the catalyst but also facilitates charge transport across the electrode/electrolyte interface. Further in-situ EIS was performed to gain deeper insight into the reaction kinetics of Ni NDC/CP and NiCe NDC/CP under operando conditions. At identical applied potentials, NiCe NDC/CP displays distinctly smaller Nyquist semicircle radii compared with Ni NDC/CP, indicative of much faster reaction kinetics during OER (Fig. 3g **and Fig. S7**). The electrochemically active surface area (ECSA) was estimated from the double-layer capacitance (C_{dl}) measurements (Fig. 3c **and Fig. S8**). NiCe NDC/CP exhibits the largest C_{dl} value (1.40 mF cm^{-2}), which is nearly twice that of Ni NDC/CP (0.73 mF cm^{-2}) and significantly higher than that of Ce NDC/CP (1.00 mF cm^{-2}). The increased C_{dl} indicates that the optimized catalyst exposes a substantially larger number of electrochemically accessible active sites, consistent with its interconnected ultrathin nanosheet architecture. To distinguish between the effects of active-site density and intrinsic catalytic activity, turnover frequency (TOF) calculations together with ECSA-normalized polarization curves were further analyzed (Figs. 3d and e). NiCe NDC/CP exhibits superior intrinsic activity even after ECSA normalization, confirming the enhanced OER performance stems from more accessible active sites and improved intrinsic activity.

Long-term operational stability was evaluated by chronopotentiometry at a practically relevant current density of 100 mA

cm^{-2} (Fig. 3h). NiCe NDC/CP maintains a nearly constant operating potential of approximately 1.53 V over 100 h of continuous electrolysis without noticeable degradation, demonstrating excellent structural robustness under prolonged anodic operation. The outstanding stability suggests that Ce effectively suppresses excessive structural reconstruction and degradation of the active NiOOH phase during long-term electrolysis. For comparison with previously reported MOF-derived OER electrocatalysts, the overpotential and Tafel slope are summarized in Fig. 3f and **Tables S2–3**. NiCe NDC/CP simultaneously achieves a low overpotential and fast reaction kinetics, placing it among the highest-performing nickel-based MOF-derived OER catalysts reported to date. Importantly, the reduced anodic overpotential and excellent stability achieved by NiCe NDC/CP are expected to provide benefits beyond laboratory-scale electrochemical performance. Lower operating voltages directly reduce the electrical energy required for water electrolysis, while enhanced durability can extend stack lifetime and decrease catalyst replacement frequency. These advantages are further quantified through the preliminary techno-economic assessment presented later, where the influence of catalyst performance on hydrogen production cost is evaluated from an industrial perspective.

3.3. Catalytic mechanism discussion

Given that MOF generally serve as precatalysts undergoing electrochemical reconstruction under alkaline OER conditions, the structural evolution of NiCe NDC during electrocatalysis was systematically investigated. The catalyst recovered after the long-term stability test was first characterized by X-ray diffraction (XRD). As shown in Fig. 4a, the diffraction peaks corresponding to the original MOF disappear completely and are replaced by reflections indexed to NiOOH (PDF# 06–0075), indicating that the NiCe NDC precursor is fully reconstructed into nickel oxyhydroxide during OER operation [48,49]. These results confirm that NiOOH is the catalytically active phase formed in situ under anodic conditions. The reconstructed catalyst was further examined by electron microscopy. As shown in Fig. 4b, the nanosheet morphology is well preserved even after prolonged electrolysis at a current density of 100 mA cm^{-2}, indicating excellent structural robustness during electrochemical reconstruction. High-resolution TEM

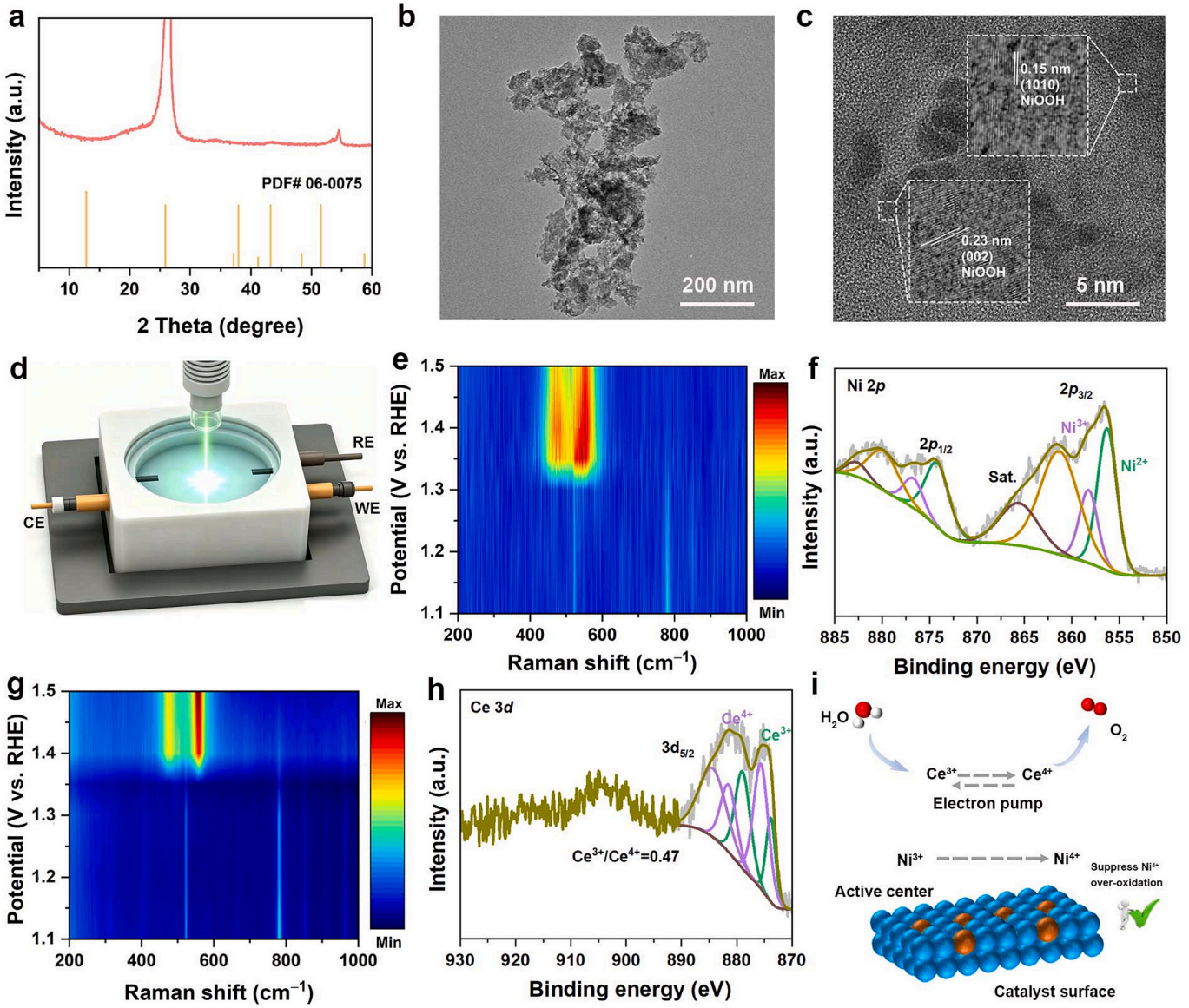

Fig. 4. (a) XRD pattern, (b) TEM, and (c) HR-TEM images of NiCe NDC/CP after OER. (d) Schematic diagram of electrochemical in-situ Raman cell. Electrochemical in-situ Raman spectra of (e) NiCe NDC/CP and (g) Ni NDC/CP in the potential range of 1.1–1.5 V (vs. RHE). (f) Ni *2p* and (h) Ce *3d* XPS spectra of NiCe NDC/CP after OER. (i) Schematic of the electron-pumping function during OER process.

(Fig. 4c) reveals clear lattice fringes that are consistent with crystalline β-NiOOH, in good agreement with the XRD results. Moreover, elemental mapping demonstrates that Ni, Ce, and O remain uniformly distributed throughout the reconstructed nanosheets after long-term operation (**Fig. S9**), suggesting that Ce remains incorporated within the reconstructed catalyst instead of undergoing segregation or dissolution. To directly monitor the reconstruction process, in situ electrochemical Raman spectroscopy was performed (Fig. 4d). Upon anodic polarization, two characteristic Raman bands located at approximately 477 and 553 cm^{-1} emerge, corresponding to the E_g bending and A_{1g} stretching modes of Ni^{3+}–O in β-NiOOH, respectively [50]. Compared with pristine Ni NDC/CP, these characteristic NiOOH signals appear at noticeably lower applied potentials for NiCe NDC/CP (Fig. 4e and g), demonstrating that Ce incorporation facilitates the electrochemical transformation of the MOF precursor into the active β-NiOOH phase. More importantly, the earlier appearance of the Raman features suggests that Ce regulates the reconstruction kinetics, enabling a more gradual and controlled phase evolution [51]. Such controlled reconstruction is expected to preserve the nanosheet architecture, maintain active-site accessibility, and suppress structural degradation that can arise from excessively rapid reconstruction. The electronic evolution of the catalyst during reconstruction was further examined by XPS. As shown in Fig. 4f, the post-reaction Ni 2*p* spectrum exhibits characteristic Ni^{3+} signals at 858.3 and 876.8 eV, confirming the formation of NiOOH during OER [52]. The residual Ni^{2+} signal is a common ex-situ relaxation phenomenon caused by ambient exposure after testing, which does not conflict with the operando phase evolution revealed by in-situ Raman. Simultaneously, the Ce 3*d* spectrum (Fig. 4h) continues to display both Ce^{3+} and Ce^{4+} species after electrolysis, while the Ce^{3+}/Ce^{4+} intensity ratio decreases from 0.59 to 0.47. This change indicates partial oxidation of Ce^{3+} during anodic polarization, consistent with previous reports showing that Ce^{3+} can be oxidized more readily than Ni^{2+} under OER conditions. The persistence of mixed-valence Ce species after prolonged operation further suggests that the Ce^{3+}/Ce^{4+} redox couple remains electrochemically active throughout the catalytic process. Based on the combined XRD, in situ Raman, TEM, and XPS results, a mechanistic model for the role of Ce during electrochemical reconstruction is proposed (Fig. 4i). The reversible Ce^{3+}/Ce^{4+} redox couple acts as a dynamic electron-buffering system during anodic polarization. With rising potential, Ce^{3+} is preferentially oxidized to Ce^{4+}, and the interconnected Ni–O–Ce network redistributes charge within the reconstructed catalyst. This dynamic electronic regulation moderates the oxidation of adjacent Ni centers, enabling controlled formation of catalytically active β-NiOOH while suppressing excessive oxidation and irreversible structural degradation. The reverse reduction of Ce^{4+} back to Ce^{3+} sustains continuous electron buffering throughout OER. Thus, Ce serves as an electronic promoter rather than an independent catalytic site, simultaneously tuning reconstruction kinetics, stabilizing the active β-NiOOH phase, and optimizing the electronic environment for oxygen evolution. This dual structural and electronic regulation accounts for the superior activity and long-term stability of the NiCe NDC.

Density functional theory (DFT) simulations were implemented to further reveal the electronic origins of improved OER activity upon Ce doping. Using evidence from in-situ Raman spectroscopy and post-reaction structural characterization, we built optimized models for reconstructed β-NiOOH and Ce-modified β-NiOOH (named Ni(*Ce*)OOH, **Fig. S10**). Ni sites were selected as reactive sites, in line with experimental results. In accordance with the experimental observations, the Ni site was selected as the catalytic center for the adsorption and transformation of the OER intermediates (*OH, *O, and *OOH) [53]. The calculated charge-density difference of Ni(Ce)OOH is presented in Fig. 5a. Pronounced charge accumulation is observed around the oxygen

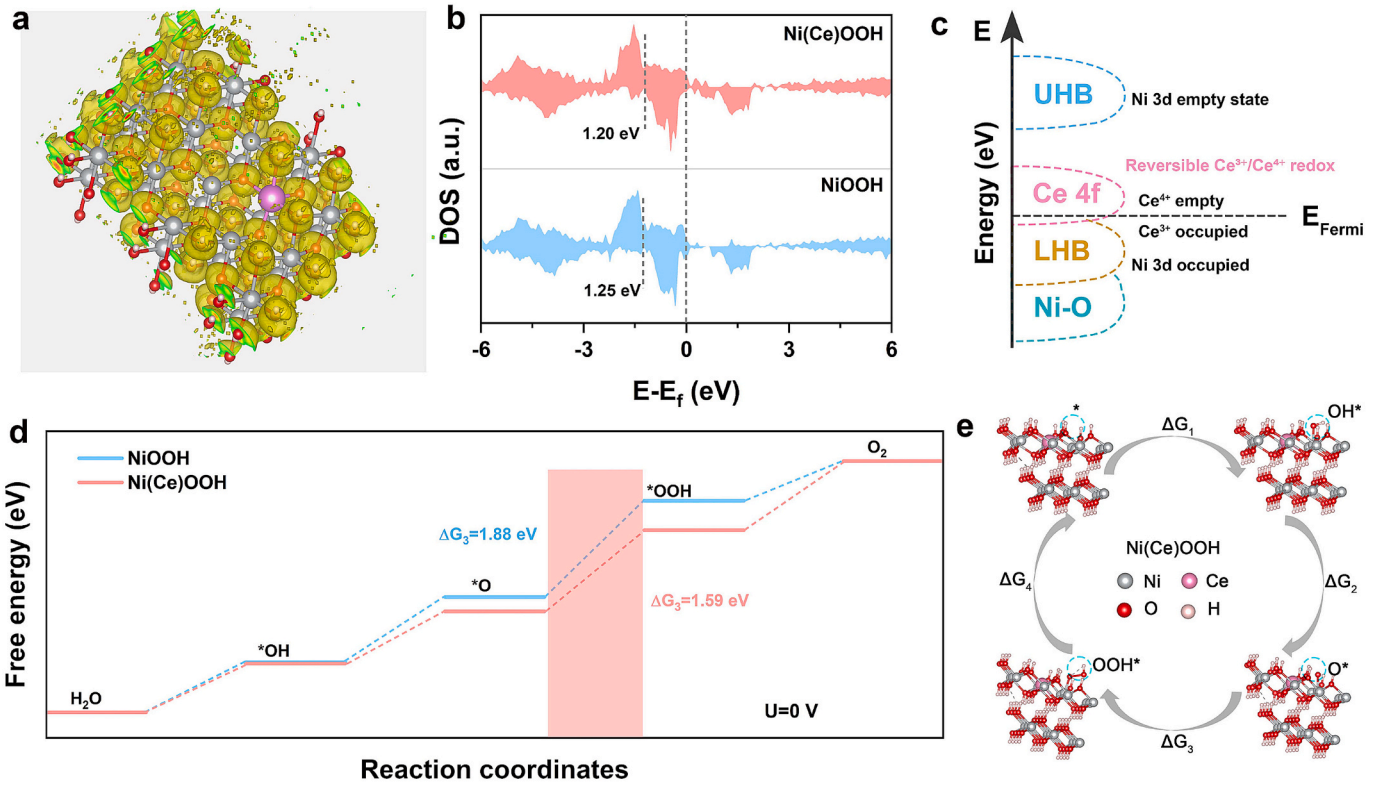

Fig. 5. (a) Spatial charge-density distribution of Ni(*Ce*)OOH. Colour code: Ni in argent, Ce in pink, O in red, H in white; electron-rich and electron-deficient regions are denoted by chartreuse and colorless shading, respectively. (b) Computed density-of-states (DOS) profiles for the Ni 3d orbital in Ni(*Ce*)OOH and pristine NiOOH. (c) Energy-level schematic for Ce-doped NiOOH. (d) OER Gibbs free-energy profiles comparing Ni(*Ce*)OOH with NiOOH. (e) Reaction-pathway schematic illustrating the OER catalytic mechanism on Ni(*Ce*)OOH. (For interpretation of the references to colour in this figure legend, the reader is referred to the web version of this article.)

atoms, whereas charge depletion occurs primarily around the neighboring Ni and Ce atoms, indicating substantial charge redistribution within the Ni-O-Ce framework [54]. This result demonstrates that Ce incorporation modifies the local electronic environment of the Ni active centers through strong metal–oxygen orbital interactions, thereby establishing an efficient electronic pathway for charge transfer during OER. The electronic density of states (DOS) further reveals the influence of Ce on the electronic structure (Fig. 5b). Both NiOOH and Ni(Ce)OOH exhibit semiconducting characteristics, whereas Ni(Ce)OOH displays a noticeably higher density of electronic states near the Fermi level. The increased DOS around the Fermi level indicates improved electronic conductivity and enhanced charge-transfer capability, which are beneficial for accelerating electrocatalytic oxygen evolution [55,56]. To further evaluate the electronic modulation induced by Ce, the d-band centers were calculated. The d-band center shifts upward from −1.25 for pristine NiOOH to −1.20 eV after Ce incorporation. According to d-band theory, this upward shift strengthens the interaction between the catalyst surface and oxygen-containing intermediates, thereby optimizing intermediate adsorption and facilitating the OER process. These results are consistent with the experimentally observed enhancement in catalytic activity.

The electronic origin of the proposed electron-buffering mechanism is further illustrated by the energy-level diagram shown in Fig. 5c. In pristine NiOOH, strong electron correlation splits Ni 3*d* states into occupied lower and unoccupied upper Hubbard bands. Upon Ce incorporation, partially occupied Ce 4*f* states emerge near the Fermi level, hosting both Ce^{3+}-related occupied levels and Ce^{4+}-related unoccupied levels to form a reversible Ce^{3+}/Ce^{4+} redox manifold. These Ce 4*f* orbitals act as dynamic electron reservoirs for reversible charge uptake and release during electrocatalysis, consistent with the mixed-valence Ce observed by XPS, and provide a microscopic explanation for the modulated Ni electronic structure and valence evolution. The OER reaction energetics were subsequently evaluated by calculating the Gibbs free-energy profiles for the elementary reaction steps at zero applied potential (Fig. 5d). For both NiOOH and Ni(Ce)OOH, the conversion of *O to *OOH exhibits the highest free-energy barrier, identifying this step as the rate-determining step (RDS). Importantly, Ni(Ce)OOH exhibits a substantially lower free-energy barrier than pristine NiOOH (Fig. 5e), demonstrating that Ce incorporation effectively facilitates the most energetically demanding step of oxygen evolution. The reduced activation barrier agrees well with the experimentally observed decrease in overpotential and Tafel slope. Combining DFT calculations with experimental observations leads to a consistent mechanistic picture. Ce doping plays a dual role in regulating both reconstruction kinetics and intrinsic catalytic activity. It lowers the energy barrier for electrochemical transformation and accelerates the reconstruction of NiCe NDC into β-NiOOH. ECSA-normalized polarization curves and TOF results further confirm that Ce enhances intrinsic activity beyond merely increasing active-site density. Ce incorporation does not simply introduce an additional catalytic site; instead, residual Ce species embedded in reconstructed β-NiOOH fundamentally regulate the local electronic environment of adjacent Ni sites. The reversible Ce^{3+}/Ce^{4+} redox couple acts as a dynamic electron-buffering system that redistributes charge across the Ni–O–Ce framework, elevates Fermi-level electron density, modulates OER intermediate adsorption-desorption, and lowers the free-energy barrier. These effects account for the experimentally observed accelerated kinetics, reduced overpotential and improved structural stability [57]. More importantly, reducing the anodic overpotential directly decreases the electrical energy required for water electrolysis, providing the fundamental scientific basis for the lower hydrogen production cost predicted by the subsequent techno-economic assessment.

3.4. Overall water splitting and techno-economic assessment

To evaluate the practical applicability of the developed OER catalyst, a two-electrode alkaline water electrolyzer was assembled using NiCe NDC/CP as the anode and commercial Pt/C/CP as the cathode (Fig. 6a). A benchmark electrolyzer employing commercial RuO_2/CP as the anode was constructed under identical conditions for comparison. As shown in Fig. 6b, the NiCe NDC/CP /$CP^{(+)}$||Pt/C/$CP^{(-)}$ electrolyzer requires cell voltages of only 1.42 and 1.57 V to deliver current densities of 10 and 100 mA cm^{-2}, respectively. These values are lower than those of the commercial $RuO_2/CP^{(+)}$||Pt/C/$CP^{(-)}$ device and compare favorably with previously reported MOF-derived alkaline water-splitting systems (Fig. 6d **and Table S4**), demonstrating the excellent overall water-splitting performance enabled by the Ce-modified NiOOH catalyst.

To further evaluate its capability under practically relevant operating conditions, the electrolyzer performance was extended to higher current densities (Fig. 6c). The assembled device requires cell voltages of 1.77 V at 500 mA cm^{-2} and 1.90 V at 1000 mA cm^{-2}, indicating that the catalyst maintains efficient reaction kinetics even under industrially relevant current densities. The relatively small increase in cell voltage with increasing current density suggests fast charge-transfer kinetics and low polarization losses, highlighting the suitability of the catalyst for high-rate hydrogen production. Long-term durability was further assessed by chronopotentiometry at 100 mA cm^{-2} (Fig. 6e). The electrolyzer retains a roughly steady operating voltage beyond 100 h, with barely observable performance decay. This outcome highlights robust structural and electrochemical durability during long-term alkaline water electrolysis. This durability is consistent with the controlled electrochemical reconstruction and dynamic electron-buffering mechanism revealed by the in situ Raman spectroscopy, XPS analysis, and DFT calculations. The combination of low operating voltage, excellent high-current-density performance, and long-term durability demonstrates that the NiCe NDC catalyst possesses considerable promise for practical alkaline water electrolysis.

Electrical energy dominates operating costs in industrial hydrogen production; reducing electrolyzer voltage thus directly lowers electricity consumption. Beyond demonstrating excellent laboratory-scale activity, this work enables a preliminary techno-economic assessment (TEA) of the noble-metal-free NiCe NDC OER catalyst for alkaline water electrolysis, using a 20 MW modular plant as the baseline. wo cathode configurations (Pt/C and commercial non-precious NiMo-type hydrogen evolution reaction (HER) catalyst) were evaluated under standardized techno-economic assumptions. The NiCe NDC‖Pt/C system operating at 1.0 A cm^{-2} (1.90 V full-cell voltage) achieved a levelized cost of hydrogen (LCOH) of USD 5.40 $kg^{-1}H_2$ with a total specific energy consumption of ~55.46 kWh $kg^{-1}H_2$, while the commercial HER cathode configuration yielded a slightly higher LCOH of USD 5.46 $kg^{-1}H_2$, as the assumed 50 mV voltage penalty elevated lifetime electricity consumption and largely offset the capital cost advantage of the non-precious cathode. Sensitivity analysis indicated that electricity price is the dominant cost driver, followed by installed capital expenditure and plant capacity factor, with cell voltage also imposing a marked influence via its control over lifelong energy consumption. Catalyst-specific comparison further confirmed that sustained reduction in cell voltage delivers substantially greater economic benefits than lowering catalyst powder cost: a 100 mV decrease in full-cell voltage reduces LCOH by approximately USD 0.15 kg^{-1} (equivalent to an annual benefit of ~USD 0.43 million for the 20 MW plant), whereas a catalyst powder cost of USD 500 kg^{-1} contributes only USD 0.0004 kg^{-1} to the final hydrogen cost. Beyond economic performance, the noble-metal-free nature of the NiCe NDC anode provides strategic value by reducing dependence on precious metal feedstocks and mitigating price volatility risks (Figs. 6f-g). It should be noted that this TEA serves as a preliminary screening analysis rather than a finalized industrial design; further pilot-scale trials and large-area electrode fabrication tests are required to fully validate industrial practicability. Nevertheless, the comprehensive electrochemical and economic evidence firmly establishes NiCe NDC as a highly promising electrocatalyst for large-scale, high-efficiency green hydrogen production.

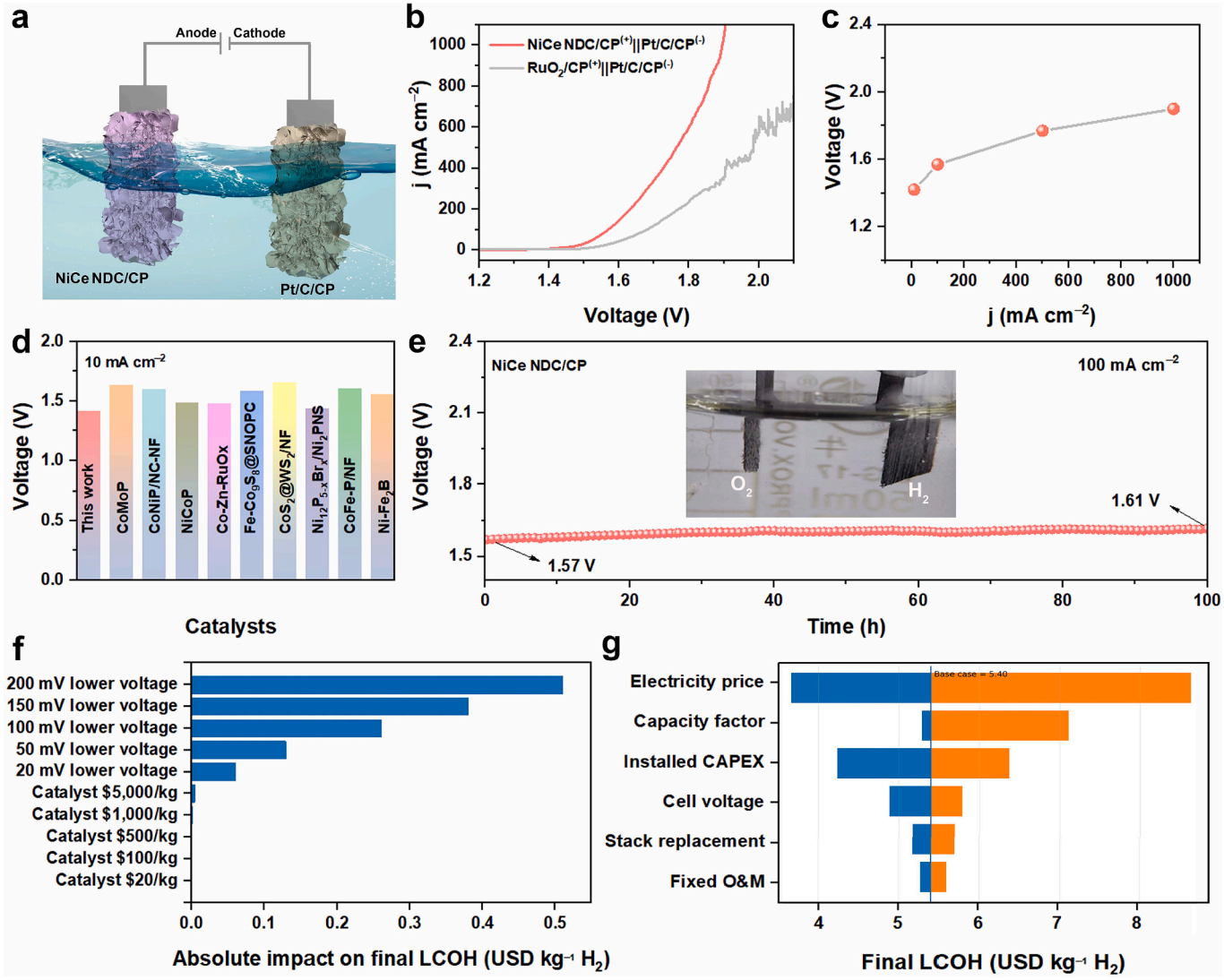

Fig. 6. (a) Schematic illustration of the assembled overall water-splitting electrolyzer. (b) Polarization curves comparing NiCe NDC/CP$^{(+)}$||Pt/C/CP$^{(-)}$ with RuO_2/CP$^{(+)}$||Pt/C/CP$^{(-)}$ recorded in 1.0 M KOH. (c) Cell-voltage versus current-density relationship for the full water-splitting device using NiCe NDC as the anode and Pt/C as the cathode. (d) Benchmarking of cell voltages at 10 mA cm^{-2} in 1.0 M KOH against recently reported electrolyzers. (e) Chronopotentiometric stability evaluation of NiCe NDC/CP$^{(+)}$||Pt/C/CP$^{(-)}$ at 100 mA cm^{-2}. (f) Comparison of the influence of NiCe NDC catalyst powder cost and sustained reductions in full-cell voltage on the final levelized hydrogen cost. (g) Combined tornado sensitivity analysis showing the effects of electricity price, installed capital expenditure (CAPEX), capacity factor, cell voltage, stack replacement, and fixed operation and maintenance (O&M) on the final levelized cost of hydrogen.

4. Conclusions

In summary, a Ce-doped Ni-based MOF (NiCe NDC) ultrathin nanosheet pre-catalyst is developed for efficient alkaline oxygen evolution, where Ce modulation concurrently tailors the electronic structure and reconstruction behavior. The Ce dopant preserves the nanosheet morphology and enables a controlled in-situ transformation to active β-NiOOH, avoiding the sluggish and disordered reconstruction of pristine Ni NDC. Mechanistically, the reversible Ce^{3+}/Ce^{4+} redox couple establishes a dynamic electronic buffering effect via Ni 3d–O 2p–Ce 4f orbital coupling, which optimizes the d-band center, facilitates charge transfer, and lowers the energy barrier of the rate-determining *O to *OOH step, with Ce acting solely as a dual electronic/structural regulator rather than a direct catalytic site. Consequently, NiCe NDC achieves a low overpotential of 194 mV at 10 mA cm^{-2} and a Tafel slope of 61.8 mV dec^{-1}, outperforming most reported MOF-derived OER catalysts. A full water-splitting electrolyzer with a Pt/C cathode delivers stable performance across a wide current range, and a preliminary techno-economic assessment for a 20 MW system projects a levelized cost of hydrogen of ~USD 5.40 kg^{-1}H_2. Distinct from conventional static modification strategies, this work establishes a dynamic rare-earth modulation approach that synergistically optimizes electronic structure and electrochemical reconstruction. Future efforts will extend this strategy to other transition-metal MOF systems and address electrode engineering and high-current-density stability under industrial conditions, advancing the practical application of MOF-derived catalysts in green hydrogen production. 20 MW system projects a levelized cost of hydrogen of approximately USD 5.40 kg^{-1}H_2.

CRediT authorship contribution statement

Haoran Yin: Writing – original draft. **Linyu Chen:** Methodology. **Linlin Huang:** Methodology. **Tayirjan Taylor Isimjan:** Conceptualization. **Dandan Cai:** Funding acquisition. **Xiulin Yang:** Funding acquisition.

Declaration of competing interest

The authors declare that they have no known competing financial interests or personal relationships that could have appeared to influence the work reported in this paper.

Acknowledgments

This work was financially supported by the Guangxi Science and Technology Projects (GUIKELT2600640010), the Natural Science Foundation of Guangxi Province (2026GXNSFBA00640178), and the National Natural Science Foundation of China (52363028; W2621022; 21965005; 22508154). Innovation Project of Guangxi Graduate Education (XYCB2025024).

Appendix A. Supplementary data

Supplementary data to this article can be found online at https://doi.org/10.1016/j.jcis.2026.141519.

Data availability

Data will be made available on request.

References

[1] W. Yu, P. Yang, F. Liu, H. Li, W. Xiao, T. Ma, G. Xu, X. Guo, D. Zhang, L. Wang, B. Li, Z. Wu, Boron vacancy enhanced Ru horizontal line Mo electron bridge as an efficient electrocatalyst for anion exchange membrane electrolysis, Adv. Mater. 38 (2026) e23202, https://doi.org/10.1002/adma.202523202.

[2] R. Jena, V. Kashyap, R. Jana, T. Mandal, T.N. Das, F.A. Rahimi, S. Barman, D. Maity, R. Kumar, D. Bhattacharyya, A. Datta, T.K. Maji, In situ tracking of Ni-MOF reconstruction into active $Ni(OH)_2$ OER catalysts, Angew. Chem. Int. Ed. 64 (2025) e202510741, https://doi.org/10.1002/anie.202510741.

[3] K. Ali, Y. Lu, M. Murad, C. Pei, Q. Liu, H.S. Park, H. Pang, X. Yu, Dimension-dependent heterostructure catalysts for acidic oxygen evolution reaction: challenges and prospects, Coord. Chem. Rev. 547 (2026) 217072, https://doi.org/10.1016/j.ccr.2025.217072.

[4] A. Shahzad, F. Zulfiqar, M. Arif Nadeem, Cobalt containing bimetallic ZIFs and their derivatives as OER electrocatalysts: a critical review, Coord. Chem. Rev. 477 (2023) 214925, https://doi.org/10.1016/j.ccr.2022.214925.

[5] J.I. Jeon, S. Jo, D. Kim, K.H. Shin, J.I. Sohn, J. Hong, Stabilizing lattice oxygen evolution with oxophilic Ce and active Ni oxide composite electrocatalysts for efficient anion exchange membrane water electrolyzers, Small 21 (2025) e2501449, https://doi.org/10.1002/smll.202501449.

[6] X. Wang, H. Zhao, X. Zhang, L. Li, W. Xiao, Q. Wu, L. Wang, Z. Wu, Strain-engineered interfacial water reorganization enables boosted HER/OER via intermediate adsorption modulation, Nano Res. Energy 5 (2026) e9120238, https://doi.org/10.26599/nre.2026.9120238.

[7] Y. Yu, Q. Wang, X. Li, Q. Xie, K. Xu, S. Zhang, H. Zhang, M. Gong, W. Lei, Laser-thermal reduction synthesis of high-entropy alloys towards high-performance pH universal hydrogen evolution reaction, Nano Mater. Sci. 7 (2025) 400–408, https://doi.org/10.1016/j.nanoms.2024.05.012.

[8] X. Fu, H. Li, Y. Zong, W. Xiao, J. Wang, H. Li, T. Ma, Z. Wu, L. Wang, Ultrafast construct local acidic microenvironment of boron-intercalated osmium with anti-precipitation and corrosion-resistant for seawater-splitting, Angew. Chem. Int. Ed. 64 (2025) e202512710, https://doi.org/10.1002/anie.202512710.

[9] Z. Wu, P. Yang, Q. Li, W. Xiao, Z. Li, G. Xu, F. Liu, B. Jia, T. Ma, S. Feng, L. Wang, Microwave synthesis of Pt clusters on black TiO_2 with abundant oxygen vacancies for efficient acidic electrocatalytic hydrogen evolution, Angew. Chem. Int. Ed. 62 (2023) e202300406, https://doi.org/10.1002/anie.202300406.

[10] T. Gao, K.S. Kumar, Z. Yan, M. Marinova, M. Trentesaux, M.A. Amin, S. Szunerits, Y. Zhou, V. Martin-Diaconescu, S. Paul, R. Boukherroub, V. Ordomsky, Covalent organic framework derived synthesis of Ru embedded in carbon nitride for hydrogen and oxygen evolution reactions, J. Mater. Chem. A 11 (2023) 19338–19348, https://doi.org/10.1039/d3ta01362f.

[11] M. Rafiq, K. Harrath, M. Feng, R. Li, A.R. Woldu, P.K. Chu, L. Hu, F. Lu, X. Yao, NixB/Mo0.8B3 nanorods encapsulated by a boron-rich amorphous layer for universal pH water splitting at the ampere level, Adv. Energy Mater. 14 (2024) 2402866, https://doi.org/10.1002/aenm.202402866.

[12] R. Deng, M. Guo, C. Wang, Q. Zhang, Recent advances in cobalt phosphide-based materials for electrocatalytic water splitting: from catalytic mechanism and synthesis method to optimization design, Nano Mater. Sci. 6 (2024) 139–173, https://doi.org/10.1016/j.nanoms.2022.04.003.

[13] W. Zhao, J. Gu, H.S. Chang, B. Deng, Y. Long, Z. Zhang, R. Ma, X. He, J. Liu, K. Huang, Y. Li, Y. Shao, H. Wu, J. Lu, Anion-regulated corrosion-driven scalable synthesis of nickel-iron electrodes for efficient oxygen evolution, Adv. Funct. Mater. 36 (2026) e28941, https://doi.org/10.1002/adfm.202528941.

[14] X. Cui, Y. Ding, F. Zhang, X. Cao, Y. Guo, L. Sun, B. Zhang, Reserved charges in a long-lived NiOOH phase drive catalytic water oxidation, Nat. Chem. 18 (2026) 120–127, https://doi.org/10.1038/s41557-025-01942-5.

[15] S. Lin, G. Han, L. Gao, G. Miao, M. Yang, J. Fu, Deep reconstruction of $Ni(OH)_2$ via magnetic-field regulation of $Fe(OH)_3$ colloids for efficient oxygen evolution reaction, Small 0 (2026) e73861, https://doi.org/10.1002/smll.73861.

[16] Y. Liu, W. Peng, H. Ma, J. Tian, K. Wang, Z. Zheng, L. Xu, Y. Ding, Tailoring electrocatalytic O(v)-NiOOH by regulating the reconstruction in Ni-based metal-organic frameworks with highly asymmetric Ni-O coordination, ACS Appl. Mater. Interfaces 17 (2025) 19806–19817, https://doi.org/10.1021/acsami.5c01983.

[17] M. Lin, T. Hu, W. Qiu, Y. Fu, Y. Wu, Y. Luo, X. Lin, Synergistic effects of Ni_2P/Ni_5P_4 heterostructure and N-doped carbon for enhanced asymmetric supercapacitor performance, Chem. Eng. J. 536 (2026) 175851, https://doi.org/10.1016/j.cej.2026.175851.

[18] R. Chen, Y. Yang, W. Wu, S. Chen, Z. Wang, Y. Zhu, N. Cheng, Reconstructed β-NiOOH enabling highly efficient and ultrastable oxygen evolution at large current density, Chem. Eng. J. 480 (2024) 148100, https://doi.org/10.1016/j.cej.2023.148100.

[19] Y. Fu, W. Qiu, S.-H. Zhou, H. Huang, Y. Luo, X. Lin, Q.-L. Zhu, First-principles calculation studies of metal-organic frameworks and their derivatives for electrochemical energy conversion and storage, Coord. Chem. Rev. 544 (2025) 216982, https://doi.org/10.1016/j.ccr.2025.216982.

[20] R.B. Ghising, U.N. Pan, M.R. Kandel, P.P. Dhakal, S. Sidra, D.H. Kim, N.H. Kim, J. H. Lee, Ruthenium single atoms implanted on NiS_2-FeS_2 nanosheet heterostructures for efficacious water electrolysis, J. Mater. Chem. A 12 (2024) 3489–3500, https://doi.org/10.1039/d3ta05630a.

[21] M. Abedi, S. Rezaee, S. Shahrokhian, Designing core-shell heterostructure arrays based on snowflake NiCoFe-LTH shelled over W_2N-WC nanowires as an advanced bi-functional electrocatalyst for boosting alkaline water/seawater electrolysis, J. Colloid Interface Sci. 666 (2024) 307–321, https://doi.org/10.1016/j.jcis.2024.04.040.

[22] W. Zhang, Y. Wang, H. Zheng, R. Li, Y. Tang, B. Li, C. Zhu, L. You, M.R. Gao, Z. Liu, S.H. Yu, K. Zhou, Embedding ultrafine metal oxide nanoparticles in monolayered metal-organic framework nanosheets enables efficient electrocatalytic oxygen evolution, ACS Nano 14 (2020) 1971–1981, https://doi.org/10.1021/acsnano.9b08458.

[23] A.-y. Lee, J. Kim, M. Pyeon, Y. Son, J. Yoo, K. Lee, Bifunctional Ni_3S_2 nanoflake/$NiMoO_4$ nanoneedle composite electrocatalysts for efficient urea oxidation and hydrogen evolution in sustainable water electrolysis, Chem. Eng. J. 512 (2025) 162044, https://doi.org/10.1016/j.cej.2025.162044.

[24] R. Abedi, G. Barati Darband, A.R. Oveisi, S. Daliran, A. Fathollahi, H. Garcia, Engineering multidimensional carbon-based electrocatalysts for water splitting: from pristine nanostructures to MOF-, POP-, and MXene-hybrids, Coord. Chem. Rev. 549 (2026) 217371, https://doi.org/10.1016/j.ccr.2025.217371.

[25] K. Yang, Y. Sun, S. Chen, M. Li, M. Zheng, L. Ma, W. Fan, Y. Zheng, Q. Li, J. Duan, Less-coordinated atomic copper-dimer boosted carbon-carbon coupling during electrochemical CO_2 reduction, Small 19 (2023) e2301536, https://doi.org/10.1002/smll.202301536.

[26] G. Ou, M. Huang, X. Lu, I. Manke, C. Yang, J. Qian, X. Lin, R. Chen, A metal-organic framework-derived strategy for constructing synergistic N-doped carbon-encapsulated NiCoP@N-C-based anodes toward high-efficient Lithium storage, Small 20 (2024) e2307615, https://doi.org/10.1002/smll.202307615.

[27] C.F. Li, L.J. Xie, J.W. Zhao, L.F. Gu, H.B. Tang, L. Zheng, G.R. Li, Interfacial Fe-O-Ni-O-Fe bonding regulates the active Ni sites of Ni-MOFs via Iron doping and decorating with FeOOH for super-efficient oxygen evolution, Angew. Chem. Int. Ed. 61 (2022) e202116934, https://doi.org/10.1002/anie.202116934.

[28] G.C. da Silva, C.S. Igel, S. Cherevko, Setting the record straight: a systematic study on Fe and Ni dissolution in NiFe-based oxygen evolution reaction catalysts, ACS Catal. 16 (2026) 8633–8641, https://doi.org/10.1021/acscatal.6c01228.

[29] M. Li, J. Yang, S. Li, L. Deng, S. Zhao, L. Li, S.F. Hung, G. Xing, T. Wang, Y. Liang, J. Ren, Y. Wu, S. Peng, Rare-earth-induced intermediate-spin co Centers in $MnCo_2O_{4.5}$ for sustainable acidic water oxidation, J. Am. Chem. Soc. 147 (2025) 45680–45690, https://doi.org/10.1021/jacs.5c17361.

[30] M. Li, W. Dong, X. Zhang, L. Xu, X. Gao, Y. Yang, Y. Tang, Y. Wang, L. Chen, G. Fu, Tuning metal/oxygen redox sequence through constructing [Eu-O-Co] unit for enhancing oxygen evolution, Adv. Funct. Mater. 35 (2025) 2507578, https://doi.org/10.1002/adfm.202507578.

[31] M. Xiao, C. Wu, J. Zhu, C. Zhang, Y. Li, J. Lyu, W. Zeng, H. Li, L. Chen, S. Mu, In situ generated layered NiFe-LDH/MOF heterostructure nanosheet arrays with abundant defects for efficient alkaline and seawater oxidation, Nano Res. 16 (2023) 8945–8952, https://doi.org/10.1007/s12274-023-5608-z.

[32] Y. Liao, Y. Xiao, Z. Li, X. Zhou, J. Liu, F. Guo, J. Li, Y. Li, Structural engineering of Co-metal-organic frameworks via Ce incorporation for improved oxygen evolution, Small (2023) e2307685, https://doi.org/10.1002/smll.202307685.

[33] P. Byaruhanga, Y. Wang, R. Tran, K.S. Choong, H. Zhong, V. Joshi, S. Song, D. Wang, M. Zou, V.G. Hadjiev, H. Guo, J. Bao, L.C. Grabow, Z. Feng, Z. Ren, S. Chen, Anion-environment-controlled synthesis of Ce-doped NiFe LDH for enhanced activity and stability in high-current-density alkaline oxygen evolution, ACS Energy Lett. 11 (2026) 2209–2219, https://doi.org/10.1021/acsenergylett.5c04101.

[34] G. Kresse, J. Furthmüller, Efficiency of ab-initio total energy calculations for metals and semiconductors using a plane-wave basis set, Comput. Mater. Sci. 6 (1996) 15–50, https://doi.org/10.1016/0927-0256(96)00008-0.

[35] G. Kresse, J. Furthmüller, Efficient iterative schemes for ab initio total-energy calculations using a plane-wave basis set, Phys. Rev. B 54 (1996) 11169–11186, https://doi.org/10.1103/PhysRevB.54.11169.

[36] J.P. Perdew, K. Burke, M. Ernzerhof, Generalized gradient approximation made simple, Phys. Rev. Lett. 77 (1996) 3865–3868, https://doi.org/10.1103/PhysRevLett.77.3865.
[37] P.E. Blöchl, Projector augmented-wave method, Phys. Rev. B 50 (1994) 17953–17979, https://doi.org/10.1103/PhysRevB.50.17953.
[38] Z. Wei, X. Wang, T. Zhu, P. Hu, L. Mai, L. Zhou, Mitigating the dissolution of V2O5 in aqueous ZnSO4 electrolyte through Ti-doping for zinc storage, Chin. Chem. Lett. 35 (2024) 108421, https://doi.org/10.1016/j.cclet.2023.108421.
[39] Y. Liao, R. He, W. Pan, Y. Li, Y. Wang, J. Li, Y. Li, Lattice distortion induced Ce-doped NiFe-LDH for efficient oxygen evolution, Chem. Eng. J. 464 (2023) 142669, https://doi.org/10.1016/j.cej.2023.142669.
[40] C. Kim, S.H. Kim, S. Lee, I. Kwon, S.H. Kim, S. Kim, C. Seok, Y.S. Park, Y. Kim, Boosting overall water splitting by incorporating sulfur into NiFe (oxy)hydroxide, J. Energy Chem. 64 (2022) 364–371, https://doi.org/10.1016/j.jechem.2021.04.067.
[41] F. Li, M. Jiang, C. Lai, H. Xu, K. Zhang, Z. Jin, Yttrium- and cerium-Codoped ultrathin metal-organic framework nanosheet arrays for high-efficiency electrocatalytic overall water splitting, Nano Lett. 22 (2022) 7238–7245, https://doi.org/10.1021/acs.nanolett.2c02755.
[42] C. Li, B. Kim, Z. Li, R. Thapa, Y. Zhang, J.M. Seo, R. Guan, F. Tang, J.H. Baek, Y. H. Kim, J.P. Jeon, N. Park, J.B. Baek, Direct electroplating ruthenium precursor on the surface oxidized nickel foam for efficient and stable bifunctional alkaline water electrolysis, Adv. Mater. 36 (2024) e2403151, https://doi.org/10.1002/adma.202403151.
[43] J. Cao, R. Zhao, L. Bai, Y. Wang, Z. Zhang, L. Wu, X. Du, J. Li, Heterogeneous engineering of nickel-iron sulfide with cerium-promoted reconstruction for enhanced oxygen evolution, Appl. Surf. Sci. 627 (2023) 157287, https://doi.org/10.1016/j.apsusc.2023.157287.
[44] H.S. Chavan, Y. Kim, S. Ha, S. Han, S. Lee, Synergistic geometric and electronic modulation in Ni–Ce layered double hydroxides for enhanced oxygen evolution reaction, J. Mater. Chem. A 14 (2026) 6354–6363, https://doi.org/10.1039/d5ta08052e.
[45] H. Sun, X. Yu, Y. Guo, J. Deng, M. Ge, Achieving efficient toluene oxidation over metal–organic framework-derived pt/CeO2-Co3O4 catalyst, Appl. Surf. Sci. 591 (2022) 153225, https://doi.org/10.1016/j.apsusc.2022.153225.
[46] K. Peng, N. Bhuvanendran, W. Zhang, S. Pasupathi, H. Su, Strong interfacial coupling activates lattice oxygen of heterogeneous cerium hydroxide/nickel ferrite catalyst for robust oxygen evolution reaction performance, Compos. Part B Eng. 309 (2026), https://doi.org/10.1016/j.compositesb.2025.113080.
[47] B. Ren, J. Huang, Q. Yuan, X. Liu, P. Li, G. Zhu, W. Xu, B. Dong, Tungsten defect-induced surface reconstruction of Ce2W2O9 arrays for enhanced oxygen evolution reaction performance, Adv. Funct. Mater. 35 (2025) 2501328, https://doi.org/10.1002/adfm.202501328.
[48] S. Hua, S.A. Shah, G.E.O. Nsang, R. Sayyar, B. Ullah, N. Ullah, N. Khan, A. Yuan, A. R. Bin Mohd Yusoff, H. Ullah, Unveiling active sites in FeOOH nanorods@NiOOH nanosheets heterojunction for superior OER and HER electrocatalysis in water splitting, J. Colloid Interface Sci. 679 (2025) 487–495, https://doi.org/10.1016/j.jcis.2024.09.219.
[49] J. Gallenberger, H. Moreno Fernández, A. Alkemper, M. Li, C. Tian, B. Kaiser, J. P. Hofmann, Stability and decomposition pathways of the NiOOH OER active phase of NiOx electrocatalysts at open circuit potential traced by ex situ and in situ spectroscopies, catalysis, Sci. Technol. 13 (2023) 4693–4700, https://doi.org/10.1039/d3cy00674c.
[50] J. Ding, D. Guo, N. Wang, H.F. Wang, X. Yang, K. Shen, L. Chen, Y. Li, Defect engineered metal-organic framework with accelerated structural transformation for efficient oxygen evolution reaction, Angew. Chem. Int. Ed. 62 (2023) e202311909, https://doi.org/10.1002/anie.202311909.
[51] J. Linke, T. Rohrbach, A.H. Clark, M. Andrzejewski, N.P.M. Casati, F.L. Buchauer, M.R. Kraglund, C. Chatzichristodoulou, E. Meade, M. Ranocchiari, T.J. Schmidt, E. Fabbri, From operando investigations to implementation of Ni-MOF-74 oxygen evolution electrocatalysts, Adv. Energy Mater. 15 (2025) 2501401, https://doi.org/10.1002/aenm.202501401.
[52] C. Mahala, M. Devi Sharma, M. Basu, Fe-doped nickel hydroxide/nickel oxyhydroxide function as an efficient catalyst for the oxygen evolution reaction, ChemElectroChem 6 (2019) 3488–3498, https://doi.org/10.1002/celc.201900857.
[53] Z. Liu, C. Yang, R. Jin, S. Li, J. Liu, J. Li, R. Yin, X. Chi, Y. Chen, L. Gao, Fe-facilitated deep reconstruction of Ni_3S_2 toward superior oxygen evolution, Carbon Energy 8 (2025) e70136, https://doi.org/10.1002/cey2.70136.
[54] M. Li, X. Wang, K. Liu, Z. Zhu, H. Guo, M. Li, H. Du, D. Sun, H. Li, K. Huang, Y. Tang, G. Fu, Ce-induced differentiated regulation of Co sites via gradient orbital coupling for bifunctional water-splitting reactions, Adv. Energy Mater. 13 (2023) 2301162, https://doi.org/10.1002/aenm.202301162.
[55] Y. Wang, Y. Zhuang, G. Yang, C. Dong, M. He, Unraveling the dynamic reconstruction of active Co(IV)-O sites on ultrathin amorphous cobalt-iron hydroxide nanosheets for efficient oxygen-evolving, Small (2024) e2404205, https://doi.org/10.1002/smll.202404205.
[56] D. Rathore, A. Banerjee, S. Pande, Bifunctional tungsten-doped $Ni(OH)_2$/NiOOH nanosheets for overall water splitting in an alkaline medium, ACS Appl. Nano Mater. 5 (2022) 2664–2677, https://doi.org/10.1021/acsanm.1c04359.
[57] L. Li, H. Xu, G. Qian, X. Cao, J. Li, Y. Xu, R. Zhang, D. Min, J. Chen, P. Tsiakaras, MoO_2-mediated Ni horizontal line Fe bond contraction and electronic modulation in Ni_3Fe alloy for efficient water electrolysis at high-current-densities, Adv. Mater. 38 (2026) e12658, https://doi.org/10.1002/adma.202512658.